Nanoscale

PAPER

View Article Online
View Journal | View Issue

Published on 06 November 2013. Downloaded by St. Petersburg State University on 13/02/2014 12:06:13.

Cite this: *Nanoscale*, 2014, **6**, 1871

Controlling the growth of porphyrin based nanostructures for tuning third-order NLO properties†

Liang Wang,[a] Yanli Chen[b] and Jianzhuang Jiang*[a]

Received 26th September 2013
Accepted 4th November 2013

DOI: 10.1039/c3nr05140d

www.rsc.org/nanoscale

A series of porphyrin nanospindles with controlled long axis length distributions of 330, 550, 800 nm, and 4 μm have been successfully fabricated *via* hierarchical self-assembly of cationic porphyrin $(H_6TPyP)^{4+}$ with the help of anionic surfactant sodium dodecyl sulfonate (SDS) due to the effective electrostatic interaction. These newly fabricated nanostructures are characterized by TEM and SEM techniques, powder X-ray diffraction analysis, electronic absorption spectroscopy, and confocal laser scanning microscopy (CLSM). The Z-scan technique with a laser duration of 5 ns at the wavelength of 532 nm reveals unreported size-dependent third-order NLO switching properties: the nonlinear absorption changes from saturation absorption to reversed saturation absorption and the nonlinear refraction from self-defocus to self-focus due to the change of the dominant scattering effect, from Rayleigh scattering for nanostructures with a smaller size than the wavelength of laser light, to Mie scattering for nanostructures with a larger size than the laser wavelength. This result is useful for the development of organic nanostructures with desired NLO properties, in particular the optical limiting properties.

Introduction

Organic nanomaterials, on the basis of functional molecular compounds with conjugated electronic structure with different morphologies and dimensions, have been fabricated through diverse methods.[1–9] Owing to their special optical, electrical, and magnetic properties associated with special electronic molecular structure, porphyrin organic nanostructures have been shown to be of significant importance because of their potential applications in the development of optoelectronic and microelectronic devices.[4,5,8–14] On the other hand, porphyrin nonlinear optical (NLO) materials have attracted significant research interests in recent years due to their fast response speed, flexibility, and facile modification with potential applications in the technology of optronics including all-optical switching, signal processing, and ultrafast optical communications.[15–27] However, early efforts made in this field seem to focus on either the bulk materials or the solution-based NLO properties with the functionality adjusted only by the molecular structure modification of the porphyrin derivatives,[15–22] which was followed by the relatively intensive investigation over the solid film materials with highly ordered molecular assemblies in recent years.[23–25] In contrast, reports on the NLO properties of organic nanostructures still remain extremely rare, limited to the nanospheres of 5,10,15,20-[1,4-benzodioxane-6-carboxalde] porphyrin arranged in both 2D and 3D arrays[26] and the nanorods self-assembled from the acidified meso-tetrakis(4-phenylsulfonicacid)porphyrin $[H_4TPPS_4]^{2-}$ and tetrakis(4-pyridyl) porphyrin tin(IV) $[SnTPyP]^{2+}$,[27] to the best of our knowledge. Towards future practical applications, investigation of the NLO properties of porphyrin nanostructures focusing on the morphology and size effects seems to be highly desired.

In the present paper, a series of porphyrin nanospindles with controlled long axis length ranging from 330, 550, 800 nm, to 4 μm have been successfully fabricated *via* hierarchical self-assembly of cationic porphyrin $(H_6TPyP)^{4+}$, Scheme 1, with the

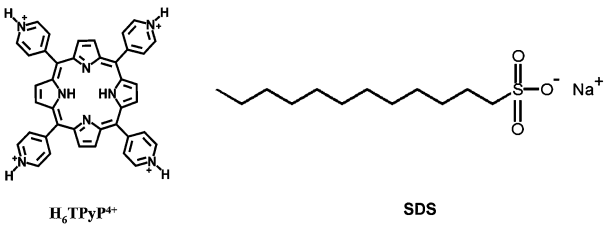

Scheme 1 Schematic molecular structures of H_6TPyP^{4+} and sodium dodecyl sulfonate (SDS).

[a]*Beijing Key Laboratory for Science and Application of Functional Molecular and Crystalline Materials, Department of Chemistry, University of Science and Technology Beijing, Beijing 100083, China. E-mail: jianzhuang@ustb.edu.cn; Fax: +86 10-6233-2462; Tel: +86 10-6233-2592*

[b]*Department of Chemistry, University of Jinan, Jinan 250022, China*

† Electronic supplementary information (ESI) available: SEM image of the shape and size evolution process of nanostructures obtained by adding SDS aqueous solution with different concentrations; electronic absorption spectra of H_6TPyP^{4+} in water and the nanostructures deposited on the quartz substrate; The CLSM fluorescence spectra of H_6TPyP^{4+} in water and the nanostructures deposited on the quartz substrate. See DOI: 10.1039/c3nr05140d

Published on 06 November 2013. Downloaded by St. Petersburg State University on 13/02/2014 12:06:13.

help of anionic surfactant sodium dodecyl sulfonate (SDS) due to the effective electrostatic interaction. These newly fabricated porphyrin nanostructures were characterized by TEM and SEM techniques, powder X-ray diffraction analysis, electronic absorption spectroscopy, and confocal laser scanning microscopy (CLSM). Most interestingly, the Z-scan technique with laser duration of 5 ns at the wavelength of 532 nm revealed unreported size-dependent third-order NLO switching properties: the nonlinear absorption changes from saturation absorption to reversed saturation absorption and the nonlinear refraction from self-defocus to self-focus due to the change of dominant scattering effect, from Rayleigh scattering for nanostructures with a smaller size than the wavelength of laser light, to Mie scattering for nanostructures with a larger size than the wavelength laser. This result is useful for the development of organic nanostructures with desired NLO properties, in particular the optical limiting properties.

Experimental

Materials and characterization

The tetrakis(4-pyridyl)porphyrin (H_2TPyP) was purchased from J & K Scientific. All the other reagents and solvents were of reagent grade and used as received. Electronic absorption spectra were recorded on a Hitachi U-4100 spectrophotometer. Confocal laser scanning microscopy (CLSM) images were acquired with a FV-1000-IX81 Olympus. Powder X-ray diffraction (PXRD) data were collected on a Shimadzu XRD-6000 diffractometer using Cu-Kα radiation ($\lambda = 1.54056$ Å) at room temperature. TEM images were measured on a JEOL JEM-2100 electron microscope operated at 200 kV. For TEM imaging, a drop of freshly prepared sample solution was cast onto a carbon copper grid.

NLO measurements. The third-order nonlinear optical (NLO) measurements were performed on nanostructures deposited on a quartz substrate using both the open-aperture and closed-aperture configuration Z-scan technique, with frequency-doubled Q-switched Nd-YAG laser (Continuum model PY61) as the light source (the pulse width of 5 ns and wavelength of 532 nm) and the incident pulse energy kept at 19 μJ in all the experiment procedure. The laser beam was focused to 30 μm at the focal point. To exclude the thermal effect, a repetition rate of 1 Hz was maintained. The spatial profiles of optical pulses were nearly Gaussian and obtained by spatial filtering. The quartz substrate with the sample was placed on a translation state controlled by a computer that moved the sample along the *Z*-axis with respect to the focal point of a 400 mm focal lens. The laser pulses adjusted by an attenuator were separated into two beams by using a splitter. The two beams were simultaneously measured by using two energy detectors (818J-09B energy probe, Newport Corporation) linked to the energy meter (model 2835-C, Newport). A personal computer was used to collect data coming from the energy meter through the RS-232C interface. For the NLO test, the suspension of the hierarchical assembly in THF was cast onto the quartz substrate forming films of thicknesses going from about 0.5 μm to 1 μm to adjust the linear transmittance of all the films to 30%. A quartz cuvette with 1 mm length of optical path was used to hold the $(H_6TPyP)^{4+}\cdot 4Cl^-$ aqueous solution, the linear transmittance of which was adjusted to 80%.

Preparation of $(H_6TPyP)^{4+}\cdot 4Cl^-$ solution and hierarchical assembly

The nanostructures were fabricated by a modified procedure over the previously reported one.[28–32] Typically, H_2TPyP (6 mg) was dissolved in hydrochloric acid (5 ml, 12 M), heated at 120 °C to dry, and kept at this temperature for further ten minutes. After being cooled to room temperature, a surfactant solution (20 ml) of different concentrations was added into $(H_6TPyP)^{4+}$ solution prepared by adding 2 ml of water into the pre-obtained green solid and shaken, resulting in a red solution, which soon turned into a cloudy brown suspension system, centrifugation of which provided $(H_6TPyP)^{4+}\cdot 4Cl^-$ hierarchically self-assembled nanostructures with the size depending on the surfactant concentration, which were washed with THF to remove surfactant molecule on the surface of the nanostructures. In the case that SDS solutions with a concentration of 0.01, 0.05, 0.15, and 0.45 mg ml^{-1} were employed, nanostructures with long axis length of 330 nm, 550 nm, 800 nm, and 4 μm were obtained, respectively. In addition, 20 ml pure water was added into the pre-obtained green solid and shaken, the resulting suspension was centrifuged three times to obtain the filtrate as an aqueous solution of $(H_6TPyP)^{4+}\cdot 4Cl^-$.

Results and discussion

A. Morphology of hierarchically self-assembled porphyrin nanospindles with controlled size: SEM and TEM observations

$(H_6TPyP)^{4+}\cdot 4Cl^-$ was produced *via* a chemical reaction route according to published procedure.[28–32] Addition of the anionic surfactant SDS aqueous solution with concentrations ranging from 0.01, 0.05, 0.15, to 0.45 mg ml^{-1} into the pre-prepared $(H_6TPyP)^{4+}\cdot 4Cl^-$ aqueous solution results in the formation of porphyrin nanospindles with the long axis length gradually increasing from 330, 550, 800 nm, to 4 μm, but the short axis length not changing significantly according to the TEM observations, Fig. 1 and S1 (ESI†). Interestingly, TEM and in particular the SEM observations reveal a slight difference in the morphology of the nanospindles with the long axis length of 4 μm from those with the long axis length of 330, 550, and 800 nm. The former nanostructures possess a flat bottom while the latter ones have a normal spindle morphology, Fig. S1 (ESI†). In addition, it is also worth noting that according to previous investigations,[33] surfactants only with concentrations larger than the critical micelle concentration (CMC), 2.4 mg ml^{-1} (9.7×10^{-3} mol l^{-1}), could be employed as effective templates to induce the formation of organic nanostructures. However, in the present case effective electrostatic interaction of the anionic surfactant SDS with cationic porphyrin chromophores $(H_6TPyP)^{4+}$ renders it possible for SDS with concentrations far below the CMC to template the self-assembly of porphyrin molecules into nanostructures.

 This journal is © The Royal Society of Chemistry 2014

Published on 06 November 2013. Downloaded by St. Petersburg State University on 13/02/2014 12:06:13.

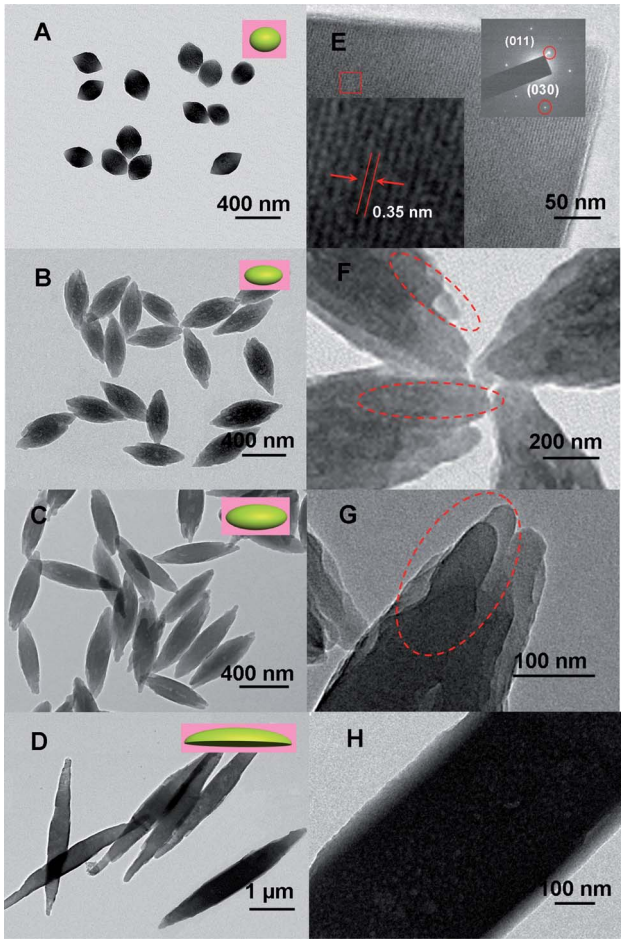

Fig. 1 TEM images of the self-assembled $(H_6TPyP)^{4+}\cdot 4Cl^-$ nanostructures obtained by adding SDS at concentrations of (A) 0.01, (B) 0.05, (C) 0.15, and (D) 0.45 mg ml^{-1} into the aqueous solution of $(H_6TPyP)^{4+}\cdot 4Cl^-$ (0.30 mg ml^{-1}) together with (E) the HRTEM image and SAED patterns of nanostructures shown in (A). (F)–(H) The magnified images of nanostructures shown in (B)–(D), respectively.

To reveal the internal structure, a magnified TEM technique was also employed. As shown in Fig. 1E, the HRTEM image of nanospindles with a long axis length of 330 nm displays well-resolved lattice fringes with an inter-planar distance of 0.35 nm, suggesting their single crystalline nature. This is supported by the bright spots observed from the selected area electron diffraction (SAED) pattern taken from a rectangular region of an individual nanospindle, shown in the inset of Fig. 1E. In addition, the *d* spacings of 1.1 and 0.44 nm deduced from the diffraction spots in the SAED pattern originating from the (011) and (030) planes, respectively, agree well with the simulated ones obtained according to X-ray diffraction analysis data of $(H_6TPyP)^{4+}\cdot 4Cl^-$ single crystals.[28] This result indicates the same crystal lattice of nanospindles with the long axis length of 330 nm with bulk single crystals. As expected, the well-resolved lattice fringes with an inter-planar distance of 0.35 nm observed in the HRTEM image of the nanospindle, Fig. 1E, are also consistent with the inter-layer distance between porphyrin chromophores in the bulk single crystals. However, different from the nanospindles with the long axis length of 330 nm, the magnified images of nanostructures with the long axis length of 550 nm, 800 nm, and 4 μm show an obviously rough surface, Fig. 1, clearly revealing that they are composed of smaller primary nanoparticles.

B. Powder X-ray diffraction analysis

To further reveal the internal structure, powder X-ray diffraction analysis has been conducted for the series of porphyrin nanostructures, Fig. 2. As can be seen, very much similar diffraction peaks were disclosed in the powder X-ray diffraction (PXRD) patterns of the four nanostructures, indicating their similar internal structure. Nevertheless, all the diffraction peaks observed in the PXRD patterns of the nanostructures match well with those in the simulated pattern obtained based on the single crystal X-ray diffraction analysis of the $(H_6TPyP)^{4+}\cdot 4Cl^-$ single crystals, Fig. 2.[28] This result not only confirms the similar internal structure of these nanostructures to single crystals but also proves the purity of the bulk phases of these nanostructures. In particular, observation of the diffraction peak at 0.44 nm (030) with relatively strong intensity associated with the porphyrin–porphyrin stacking distance according to the single crystal X-ray crystallographic analysis, suggests the favorable molecular packing in the co-facial conformation depending mainly on the π–π interaction between porphyrin rings in these nanostructures. This result is consistent with their aggregation behavior deduced from electronic absorption spectroscopy (*vide infra*). At the end of this section, it is worth noting that the three well-defined peaks due to the (001), (0$\bar{1}$1), and (002) planes in the simulated pattern have not been revealed in the PXRD patterns of porphyrin nanostructures, indicating the different preferential growth directions of the nanostructures from single crystals. Additional support for this comes from the obvious difference in the peak intensity between the nanostructure PXRD patterns and the simulated one, Fig. 2.

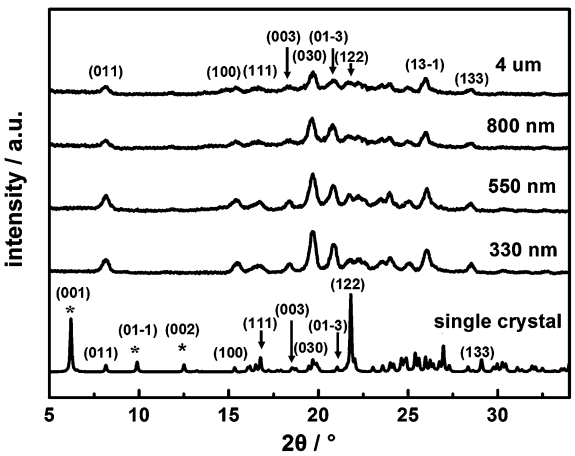

Fig. 2 X-ray diffraction patterns of the $(H_6TPyP)^{4+}\cdot 4Cl^-$ nanostructures with the long axis length of 330 nm, 550 nm, 800 nm, and 4 μm, together with the simulated one obtained on the basis of the X-ray diffraction analysis result for $(H_6TPyP)^{4+}\cdot 4Cl^-$ single crystals.

Published on 06 November 2013. Downloaded by St. Petersburg State University on 13/02/2014 12:06:13.

C. Electronic absorption spectroscopy

Electronic absorption spectroscopic measurement was also carried out to reveal the packing mode of the hierarchically self-assembled porphyrin nanostructures. As shown in Fig. S2 (ESI†), the nanospindles with different sizes show very much similar electronic absorption spectra, indicating their similar internal molecular arrangement. In comparison with the spectrum of metal free $(H_6TPyP)^{4+}\cdot 4Cl^-$ in aqueous solution, both the Soret and Q bands of the nanostructures show a significant blue-shift from 441 to 413 nm and from 516–640 to 493–607 nm, respectively, suggesting the formation of *H*-aggregates in these nanostructures due to the face-to-face π–π interaction between the porphyrin skeletons according to the exciton theory.[4,5,34]

D. Confocal laser scanning microscopy (CLSM) images of the porphyrin nanostructures

Confocal laser scanning microscopy (CLSM) was also employed to characterize the porphyrin nanostructures. Fig. 3 shows the fluorescence images of the porphyrin nanostructures with the long axis length of 330 nm, 550 nm, 800 nm, and 4 μm. All of these exhibit strong typical red fluorescence emission of porphyrins when excited with the laser light at 330–380 nm, indicating the good emitter role of these nanostructures. Interestingly, as shown in Fig. 3, within the resolution of the optical microscope, the gradual increase in the particle size of the series of porphyrin nanostructures can be clearly distinguished. In addition, fluorescence spectroscopic measurements were also carried out. Fig. S3 (ESI†) shows the CLSM fluorescence spectra of the series of four nanostructures deposited on the quartz substrate together with the fluorescence spectrum of H_6TPyP^{4+} in water as a reference with an excitation wavelength of 412 and 430 nm for the nanostructures and solution sample, respectively. As can be seen from this figure, H_6TPyP^{4+} in water displays two emission bands at 648 and 705 nm, respectively. This appears also true for the prophyrin nanostructures deposited on the quartz substrate. Despite the slight decrease in the fluorescence intensity for all the porphyirn nanostructures in comparison with the H_6TPyP^{4+} solution sample, owing to the excitonic coupling between the porphyrin molecules, there seems to be no significant change in terms of the emission band position in the fluorescence spectra of the nanostructures along with the increase in their long axis length.

E. Time-dependent self-assembling process of the hierarchically self-assembled nanostructures

For the purpose of understanding the self-assembly mechanism, the time-dependent self-assembling process of the system obtained at the SDS concentration of 0.45 mg ml^{-1} was monitored by TEM, Fig. 4. As can be seen in Fig. 4A and D, spherical primary nano-particles with an average diameter of 200 nm start to appear after 10 s after the addition of SDS into the H_6TPyP^{4+} solution. Along with the increase in the reaction time from 10 s to 20 s, 40 s, and 50 s, these spherical primary nano-particles gradually link together by fusion, Fig. 4B, C, and H, forming the nanospindles. The result also clearly reveals the formation of porphyrin nanostructures in a hierarchically self-assembling manner. Fortunately, a spindle-like super-nanostructure composed of two spindles with a crackle at the center part was found to co-exist with other normal nanospindles, Fig. 4I. Obviously, the spindle-like porphyrin nanostructures with a flat bottom are formed due to the cracking of the spindle-like super-nanostructure into two separate parts, Fig. 4H. Interestingly, observation of the intermediate hierarchically self-assembled nanostructures in which the primary nano-particles share the same smooth bottom surface during the formation process as displayed in Fig. 4D–F and H suggests the self-assembly of the primary nano-particles with the SDS aggregate as a template

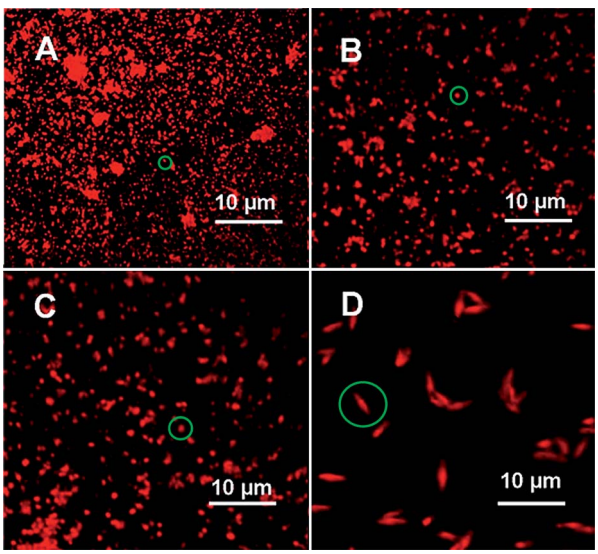

Fig. 3 CLSM images of the nanostructures with a long axis length of 330 nm (A), 550 nm (B), 800 nm (C), and 4 μm (D) deposited on a quartz substrate with an excitation wavelength of 330–380 nm.

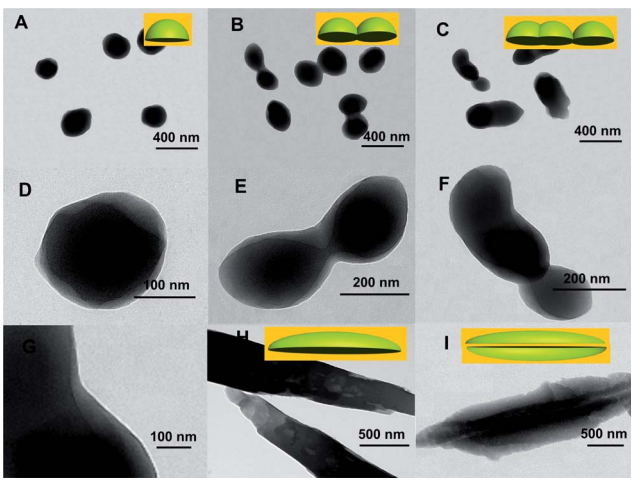

Fig. 4 TEM images of time resolved transformation of nano-structures obtained with SDS (0.45 mg ml^{-1}) and H_6TPyP^{4+} (0.30 mg ml^{-1}) after (A) 10 s, (B) 20 s, (C) 40 s, and (H and I) 50 s, respectively, for addition of SDS solution together with the magnified images for the nanostructures shown in A (D), B (E), and C (F and G).

This journal is © The Royal Society of Chemistry 2014

Published on 06 November 2013. Downloaded by St. Petersburg State University on 13/02/2014 12:06:13.

instead of being randomly connected. In addition, the spindle-like super-nanostructure composed of two spindles observed actually gives a hint of the spindle-like double-layer structure of the surfactant aggregate template as detailed below.

F. Formation mechanism of the porphyrin nanostructures

On the basis of the above mentioned experimental results, the formation mechanism of the porphyrin nanospindles as exemplified by those with a flat bottom obtained from the system at the SDS concentration of 0.45 mg ml^{-1} was proposed and shown in Fig. 5. In this system, the SDS molecules themselves first start to aggregate into both smaller spherical loose SDS aggregates and larger spindle-like SDS aggregates with a double-layered structure according to both TEM, SEM, and time-dependent observations as detailed above, Fig. 5A and 6D. Then the porphyrin molecules $(H_6TPyP)^{4+}$ were adsorbed onto the surface of the small spherical SDS aggregates due to their larger surface energy than the larger ones (depending on the effective electrostatic interaction) and form a core, Fig. 5B. Continuous self-assembly of porphyrin molecules on the surface of the core *via* synergetic interactions among hydrogen-bonding, π–π stacking, and ion pairing, led to the formation of the primary nano-particles as observed in Fig. 4A. In the following stage, the primary nano-particles with a positive charge were adsorbed onto the surface of the larger spindle-like double-layered SDS aggregates with a negative charge and further fused together to form the super-nanostructures composed of two spindles, Fig. 5C–E, each of which then breaks into two nanospindles with a flat bottom as the target nanostructures obtained from this system, Fig. 5F, when the tension between the pair of two spindles exceeds the van der Waals' force between the double layered SDS structure. As for the reaction system with the SDS concentration of 0.01 mg ml^{-1}, formation of the smaller spindle-like SDS aggregates as the sole template at the beginning of reaction is responsible for the isolation of smaller porphyrin nanospindles with normal morphology from this system, Fig. 6A. Along with the increase of the SDS concentration to 0.05 mg ml^{-1}, simultaneous formation of both the smaller and large spindle-like SDS aggregates directs the formation of larger porphyrin nanospindles, also with normal morphology, Fig. 6B. This should be also true for the system with the SDS concentration of 0.15 mg ml^{-1}, Fig. 6C.

G. Size-dependent third-order nonlinear optical (NLO) properties

By detecting the far-field sample transmittance of a focused Gaussian beam as a function of sample position (Z), the Z-scan technique provides not only nonlinear absorption and refraction information but also the sign of nonlinearity, an important parameter for optical signal processing devices which can only be obtained by this technique. In the present case, Z-scan measurements under both open-aperture and closed-aperture configurations were first carried out over the aqueous solution sample of $(H_6TPyP)^{4+}$ in a quartz cell at 532 nm with a laser duration of 5 ns. Then comparative studies were conducted over the porphyrin nanostructures deposited on the quartz substrate. Fig. 7A compares the Z-scan data of the aqueous solution sample of $(H_6TPyP)^{4+}$ and the nanospindles with the long axis length of 330 nm collected under an open-aperture configuration. The fitting curves obtained on the basis of a five-level energy model which took into account the dynamic thermal effect resulting from the transient excited-state absorption according to the literature method are also given in Fig. 7A.[35] In line with previous reports,[25] the $(H_6TPyP)^{4+}$ solution exhibits relatively weak reverse saturation absorption (RSA) resulting from the excited-state absorption. In contrast, the nanospindles with the long axis length of 330 nm displays strong saturation absorption (SA), due mainly to the dominant nonlinear Rayleigh scattering from the scattering centers in the

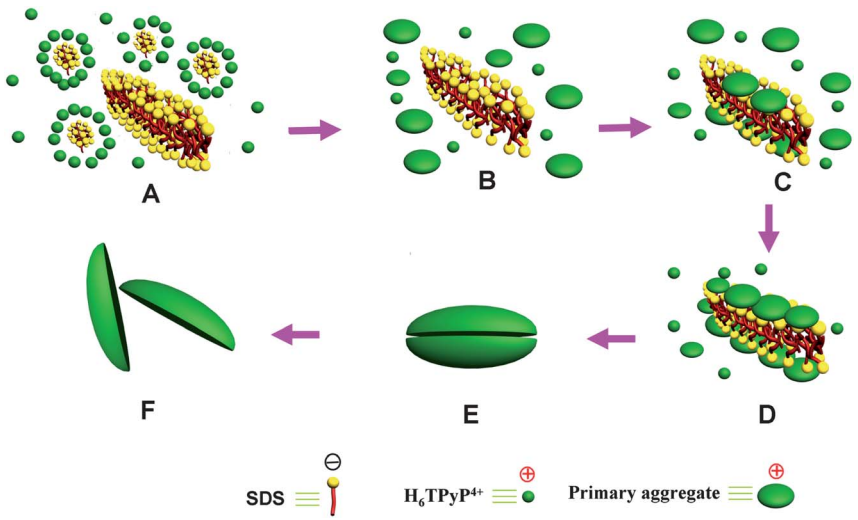

Fig. 5 The formation mechanism of the hierarchically self-assembled $(H_6TPyP)^{4+}\cdot 4Cl^-$ nanospindles with a flat bottom from the system with the SDS concentration of 0.45 mg ml^{-1}.

Published on 06 November 2013. Downloaded by St. Petersburg State University on 13/02/2014 12:06:13.

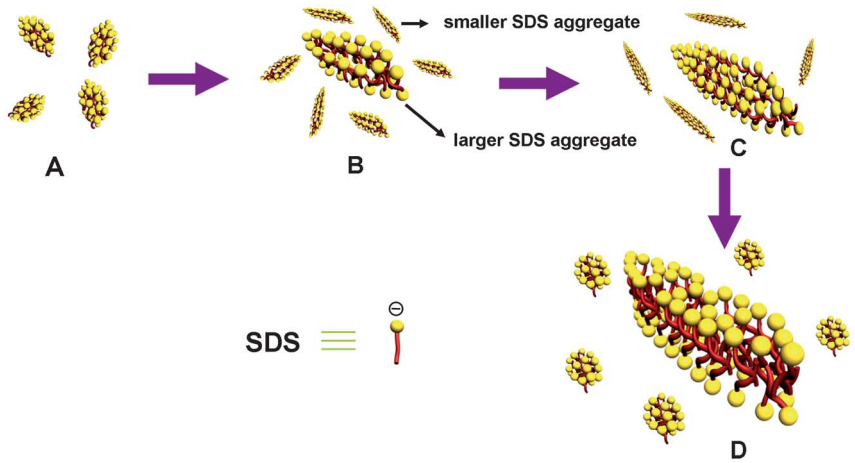

Fig. 6 Schematic illustration of the shape evolution process of the surfactant aggregates along with increases of the SDS concentration from 0.01 (A), 0.05 (B), 0.15 (C), to 0.45 mg ml^{-1} (D).

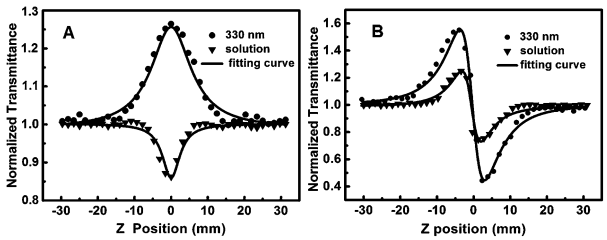

Fig. 7 (A) Normalized Z-scan transmittance curves collected under an open-aperture configuration and (B) closed-aperture configuration, respectively, for the aqueous solution sample of $(H_6TPyP)^{4+}$ in the quartz cell and the porphyrin nanospindles with an axis length of 330 nm deposited on a quartz substrate with a laser duration of 5 ns at the wavelength of 532 nm, together with the fitting curves obtained on the basis of a five-level energy model according to the literature method.[35]

nanostructures over the excited-state absorption of porphyrin molecules because of the small size of nanostructures, 330 nm, in comparison with the laser wavelength of 532 nm together with the negligible resonance enhancement effect due to the relatively weak absorption at 532 nm (which lies just on the shoulder of the main linear absorption band for both the aqueous solution and nanostructure samples).[25] According to eqn (1) (ref. 35) and on the basis of the experimental results, the nonlinear absorption coefficients are calculated to be $\beta_{\text{in water}} = 5.1 \times 10^{-9}$ and $\beta_{330\ \text{nm}} = -7.1 \times 10^{-7}$ m W^{-1}, respectively.

$$T(z) = \frac{1}{\sqrt{\pi}q(z)} \int_{-\infty}^{\infty} \ln[1 + q(z)]e^{-\tau^2} d\tau$$
$$q(z) = \alpha_2^{\text{eff}} I(z) \frac{1 - e^{-\alpha_0 L}}{\alpha_0} \quad (1)$$

where α_0 and α_2 are linear and effective third-order NLO absorptive coefficients, τ is the time, L is the optical path and $I(z)$ is the input laser intensity at position Z. The light transmittance (T) is a function of the sample's Z position (with respect to the focal point at $Z = 0$).

Fig. 7B displays the NLO refractive data for the aqueous solution sample of $(H_6TPyP)^{4+}$ in a quartz cell and the nanospindles with a long axis length of 330 nm deposited on a quartz substrate collected under closed-aperture configuration. As can be expected from the absorptive nonlinearity result, the peak-valley pattern of the normalized transmittance curve for the aqueous solution sample of $(H_6TPyP)^{4+}$ shows a negative sign for the nonlinear refraction and exhibits a weak self-defocusing behavior of propagating light in this sample. The peak and valley position are located at −3.3 before the focus and 2.0 behind the focus, leading to the unsymmetrical peak-valley position of the normalized transmittance with respect to the focus ($Z = 0$) for the porphyrin aqueous solution due to the electron cloud distortion of the porphyrin molecules.[36] Interestingly, the peak-valley pattern of the normalized transmittance curve for the nanostructures with the long axis length of 330 nm also show a negative sign for the nonlinear refraction, which however exhibits an enhanced self-defocusing behavior due mainly to the dominant nonlinear Rayleigh scattering from the scattering centers in the nanostructures over the electron cloud distortion of the porphyrin molecules associated with the small size of nanostructures, 330 nm, in comparison with the laser wavelength of 532 nm,[37] Fig. 7B. The peak and valley positions are located at −4.0 before the focus and 2.8 behind the focus, respectively, also resulting in an unsymmetrical peak-valley position of the normalized transmittance with respect to the focus ($Z = 0$) for these nanostructures. On the basis of these experimental results and according to eqn (2),[35] the third-order nonlinear refractive indexes are calculated to be $n_{2\ \text{in water}} = -4.0 \times 10^{-16}$ and $n_{2\ 330\ \text{nm}} = -4.0 \times 10^{-13}$ m^2 W^{-1}, respectively.

$$n_2 = \frac{\lambda\alpha_0}{0.812\pi I(1 - e^{-\alpha_0 L})} \Delta T_{v-p} \quad (2)$$

where ΔT_{v-p} is the difference between the normalized transmittance values at the valley and peak portions, I is the peak irradiation intensity at focus, and λ is the wavelength of the laser.

This journal is © The Royal Society of Chemistry 2014

Published on 06 November 2013. Downloaded by St. Petersburg State University on 13/02/2014 12:06:13.

To clarify the effect of the size of the nanostructures on their third-order optical nonlinearities, Fig. 8A compares the NLO absorptive properties of the nanospindles with the long axis length (330, 550, 800 nm, and 4 μm). As detailed above, the nanospindles with a long axis length of 330 nm display typical saturation absorption (SA) behavior. However, when the nanostructures with the long axis length reach 4 μm, the nanospindles exhibit typical reversed saturation absorption (RSA) behavior, Fig. 8A. This result is explained by the observation of the obvious transition state from SA to RSA of the third-order NLO absorptive properties for the nanostructures with long axis lengths of 550 and 880 nm, Fig. 8A. Accordingly, the nonlinear absorptive coefficient for the nanostructures with the long axis length of 4 μm was also calculated with the value of $\beta_{4\ \mu m} = 3.7 \times 10^{-7}$ m W^{-1}, in comparison with the one of $\beta_{330\ nm} = -7.1 \times 10^{-7}$ m W^{-1}. Due to their transition (from SA to RSA) third-order NLO absorption behavior, calculation over the nonlinear absorptive coefficients for the nanostructures with long axis lengths of 550 and 880 nm is impossible.

In a similar manner, Fig. 8B compares the third-order NLO refractive properties of the whole series of nanostructures. To repeat the fact, the peak-valley pattern of the normalized transmittance curves reveals that the nanostructures with a long axis length of 330 nm show a negative sign for the nonlinear refraction, indicating the characteristic self-defocusing behavior of propagating light in this sample. However, along with the increase in the particle size to a size comparable with the laser wavelength, the transmission rate for the nanospindles with the long axis length of 550 nm is decreased owing to the emergence of t nonlinear Mie-scattering in the nanostructures despite the sign of the nonlinear refraction remaining unchanged, Fig. 8B. Further increases in the nanoparticle size leads to a further strengthening of the nonlinear Mie-scattering, resulting in a further decreased transmission rate for the nanospindles with the long axis length of 800 nm with the sign of the nonlinear refraction also remaining unchanged, Fig. 8B. When the nanostructure size is further increased to 4 μm, which far exceeds the laser wavelength of 532 nm, the Mie-scattering effect gets significantly enhanced and dominates the NLO behavior of the nanostructures instead of the Rayleigh scattering effect, resulting in the change of refractive behavior of this species of porphyrin nanostructures from a characteristic self-defocusing behavior to a self-focusing one with the sign changing from negative to positive, Fig. 8B. A theoretical treatment as detailed above according to eqn (2) provides the third-order nonlinear refractive indexes: $n_{2\ 330\ nm} = -4.0 \times 10^{-13}$, $n_{2\ 550\ nm} = -2.9 \times 10^{-13}$, $n_{2\ 800\ nm} = -1.2 \times 10^{-13}$, and $n_{2\ 4\ \mu m} = 4.8 \times 10^{-13}$ m^2 W^{-1}. These results clearly reveal the important role of nanostructure size in controlling the third-order NLO properties of organic nanomaterials.

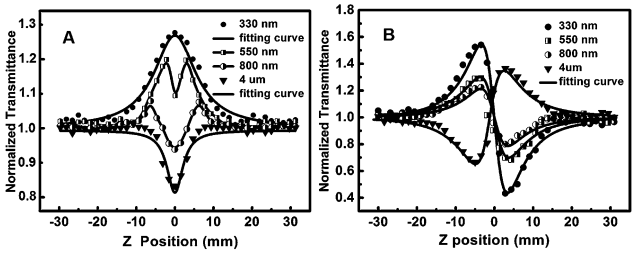

Fig. 8 (A) Normalized *Z*-scan transmittance curves collected under an open-aperture configuration and (B) closed-aperture configuration, respectively, for nanostructures with long axis lengths of 330 nm, 550 nm, 800 nm, and 4 μm deposited on a quartz substrate with a laser duration of 5 ns at the wavelength of 532 nm, together with the fitting curves obtained on the basis of a five-level energy model according to the literature method.[35]

Conclusions

In conclusion, a series of porphyrin nanostructures with controlled size were successfully fabricated *via* hierarchical self-assembly of cationic porphyrin $(H_6TPyP)^{4+}$ with the help of the anionic surfactant SDS. Z-scan technique experiments revealed the size-dependent third-order NLO switching properties of these organic nanostructures. Along with the increase in the nanostructure size, the nonlinear absorption changes from saturation absorption to reversed saturation absorption and the nonlinear refractive property from self-defocus to self-focus. This represents the first observation of the size dependent third-order NLO switching property of organic nanostructures, to the best of our knowledge. The present result should be useful for the development of organic nanostructures with desired NLO properties.

Acknowledgements

Financial support from the National Key Basic Research Program of China (Grant nos 2013CB933402 and 2012CB224801), Natural Science Foundation of China, Beijing Municipal Commission of Education, and University of Science and Technology Beijing is gratefully acknowledged.

Notes and references

1 M. Mas-Torrent and C. Rovira, *Chem. Rev.*, 2011, **111**, 4833.
2 Z. Q. Lin, P. J. Sun, Y. Y. Tay, J. Liang, Y. Liu, N. E. Shi, L. H. Xie, M. D. Yi, Y. Qian, Q. L. Fan, H. Zhang, H. H. Hng, J. Ma, Q. Zhang and W. Huang, *ACS Nano*, 2012, **6**, 5309.
3 L. T. Kang, Z. C. Wang, Z. W. Cao, Y. Ma, H. B. Fu and J. N. Yao, *J. Am. Chem. Soc.*, 2007, **129**, 7305.
4 Y. Gao, X. Zhang, C. Ma, X. Li and J. Jiang, *J. Am. Chem. Soc.*, 2008, **130**, 17044.
5 G. Lu, Y. Chen, Y. Zhang, M. Bao, Y. Bian, X. Li and J. Jiang, *J. Am. Chem. Soc.*, 2008, **130**, 11623.
6 Y. Zhang, P. Chen, L. Jiang, W. Hu and M. Liu, *J. Am. Chem. Soc.*, 2009, **131**, 2756.
7 T. Wang, J. Jiang, Y. Liu, Z. Li and M. Liu, *Langmuir*, 2010, **26**, 18694.
8 F. Bai, Z. Sun, H. M. Wu, R. E. Haddad, E. N. Coker, J. Y. Huang, M. A. Rodriguez and H. Y. Fan, *Nano Lett.*, 2011, **11**, 5196.

Published on 06 November 2013. Downloaded by St. Petersburg State University on 13/02/2014 12:06:13.

9 Y. F. Qiu, P. L. Chen and M. H. Liu, *J. Am. Chem. Soc.*, 2010, **132**, 9644.
10 P. Ma, Y. Chen, Y. Bian and J. Jiang, *Langmuir*, 2010, **26**, 3678.
11 Q. Wang, Y. Chen, P. Ma, J. Lu, X. Zhang and J. Jiang, *J. Mater. Chem.*, 2011, **21**, 8057.
12 H. Liu, J. Xu, Y. Li and Y. Li, *Acc. Chem. Res.*, 2010, **43**, 1496.
13 K. Iliopoulos, A. El-Ghayoury, H. E. Ouazzani, M. Pranaitis, E. Belhadj, E. Ripaud, M. Mazari, M. Sallé, D. Gindre and B. Sahraoui, *Opt. Express*, 2012, **20**, 25311.
14 J. Xu, S. Semin, D. Niedzialek, P. H. J. Kouwer, E. Fron, E. Coutino, M. Savoini, Y. Li, J. Hofkens, H. Uji-I, D. Beljonne, T. Rasing and A. E. Rowan, *Adv. Mater.*, 2013, **25**, 2084.
15 T. V. Duncan, K. Song, S. T. Hung, I. Miloradovic, A. Nayak, A. Persoons, T. Verbiest, M. J. Therien and K. Clays, *Angew. Chem., Int. Ed.*, 2008, **47**, 2978.
16 T. Xu, S. P. Wu, I. Miloradovic, M. J. Therien and J. K. Blasie, *Nano Lett.*, 2006, **6**, 2387.
17 T. Ishizuka, L. E. Sinks, K. Song, S. T. Hung, A. Nayak, K. Clays and M. J. Therien, *J. Am. Chem. Soc.*, 2011, **133**, 2884.
18 J. E. Raymond, A. Bhaskar, T. Goodson III, N. Makiuchi, K. Ogawa and Y. Kobuke, *J. Am. Chem. Soc.*, 2008, **130**, 17212.
19 M. O. Senge, M. Fazekas, E. G. A. Notaras, W. J. Blau, M. Zawadzka, O. B. Locos and E. M. N. Mhuircheartaigh, *Adv. Mater.*, 2007, **19**, 2737.
20 N. Jiang, G. Zuber, S. Keinan, A. Nayak, W. Yang, M. J. Therien and D. N. Beratan, *J. Phys. Chem. C*, 2012, **116**, 9724.
21 P. Aloukos, K. Iliopoulos, S. Couris, D. M. Guldi, C. Sooambar, A. Mateo-Alonso, P. G. Nagaswaran, D. Bonifazi and M. Prato, *J. Mater. Chem.*, 2011, **21**, 2524.
22 E. Xenogiannopoulou, M. Medved, K. Iliopoulos, S. Couris, M. G. Papadopoulos, D. Bonifazi, C. Sooambar, A. Mateo-Alonso and M. Prato, *ChemPhysChem*, 2007, **8**, 1056.
23 S. Biswas, H. Y. Ahn, M. V. Bondar and K. D. Belfield, *Langmuir*, 2012, **28**, 1515.
24 P. K. Pandey, C. S. S. Sandeep, R. Philip and V. Lakshminarayanan, *J. Phys. Chem. C*, 2009, **113**, 8630.
25 L. Jiang, F. S. Lu, H. M. Li, Q. Chang, Y. L. Li, H. B. Liu, S. Wang, Y. L. Song, G. L. Cui, N. Wang, X. R. He and D. B. Zhu, *J. Phys. Chem. B*, 2005, **109**, 6311.
26 C. Huang, Y. Song, Y. Li, H. Liu and D. Zhu, *Adv. Mater.*, 2010, **22**, 3532.
27 N. Mongwaketsi, S. Khamlich, M. Pranaitis, B. Sahraoui, F. Khammar, G. Garab, R. Sparrow and M. Maaza, *Mater. Chem. Phys.*, 2012, **134**, 646.
28 L. Wang, Y. Chen, Y. Bian and J. Jiang, *J. Phys. Chem. C*, 2013, **117**, 17352.
29 E. Fleischer, *Inorg. Chem.*, 1962, **1**, 493.
30 E. Fleischer and A. L. Stone, *Chem. Commun.*, 1967, 332.
31 A. Stone and E. B. Fleischer, *J. Am. Chem. Soc.*, 1968, **90**, 2735.
32 E. B. Fleischer and L. E. Webb, *Inorg. Chem.*, 1962, **1**, 493.
33 H. Yan, X. L. Guo, S. L. Yuan and C. B. Liu, *Langmuir*, 2011, **27**, 5762.
34 S. Verma, A. Ghosh, A. Das and H. N. Ghosh, *J. Phys. Chem. B*, 2010, **114**, 8327.
35 M. S. Bahae, A. A. Said, T. H. Wei, D. J. Hagan and E. W. V. Stryland, *IEEE J. Quantum Electron.*, 1990, **26**, 760.
36 Z. B. Liu, Y. Z. Zhu, Y. Zhu, S. Q. Chen, J. Y. Zheng and J. G. Tian, *J. Phys. Chem. B*, 2006, **110**, 15140.
37 S. M. O. Flaherty, R. Murphy, S. V. Hold, M. Cadek, J. N. Coleman and W. J. Blau, *J. Phys. Chem. B*, 2003, **107**, 958.

This journal is © The Royal Society of Chemistry 2014